ACS SENSORS

pubs.acs.org/acssensors

Article

Diffusion-Induced Ingress of Angiotensin-Converting Enzyme 2 into the Charge Conducting Path of a Pentacene Channel for Efficient Detection of SARS-CoV-2 in Saliva Samples

Ajoy Mandal, Samik Mallik, Sovanlal Mondal, Suvani Subhadarshini, Riya Sadhukhan, Tanmay Ghoshal, Suman Mitra, Mousam Manna, Suman Mandal, and Dipak K. Goswami*

Cite This: https://doi.org/10.1021/acssensors.2c01287

Read Online

ACCESS | Metrics & More | Article Recommendations | Supporting Information

ABSTRACT: Rapid and accurate identification of a pathogen is crucial for disease control and prevention of the epidemic of emerging infectious like SARS-CoV-2. However, no foolproof gold standard assay exists to date. Nucleic acid-based molecular diagnostic tests have been established for identifying COVID-19. However, viral RNAs are highly unstable in handling with poor laboratory procedures, leading to a false negative that accelerates the spread of the disease. Detection of the spike protein (S1) of the SARS-CoV-2 virus through a proper receptor, commonly used in antigen-based rapid testing kits, also suffers from false-negative predictions due to decreasing viral titers in clinical specimens. Organic field-effect transistor (OFET)-based sensors can be highly sensitive upon properly integrating receptors in the conducting channel. This work demonstrates how angiotensin-converting enzyme 2 (ACE2) molecules can be used as receptor molecules of the SARS-CoV-2 virus in the OFET platform. Integration of ACE2 molecules into pentacene grain boundaries has been studied through the statistical analysis of rough surfaces in terms of lateral correlation length and interface width. The uniform coating of ACE2 molecules has been confirmed through growth studies to achieve better ingress of the receptors into the conducting channel at the semiconductor/dielectric interface of OFETs. We have observed less than a minute detection time with 94% sensitivity, which is the highest reported value. The sensor works with a saliva sample, requiring no sample preparation or virus transfer medium. A prototype module developed for remote monitoring confirms the suitability for point-of-care (POC) application at large-scale testing in more crowded areas like airports, railway stations, shopping malls, etc.

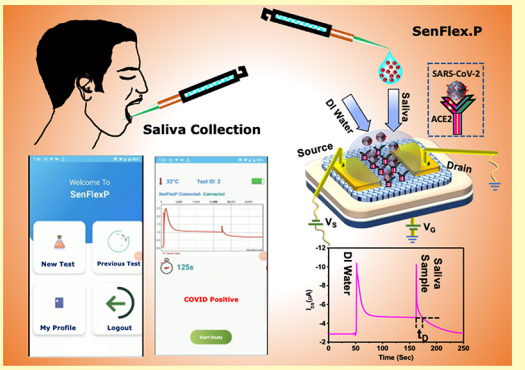

KEYWORDS: *COVID-19, SARS-CoV-2, field-effect transistor, angiotensin-converting enzyme 2 (ACE2), biosensor*

The massive impact of coronavirus (COVID-19) infection on human health has continued through new mutants since its outbreak in 2019.[1,2] Although the mortality rate has subsided in the recent mutants, the disease predominantly affects the respiratory system, leading to many pulmonary dysfunction-related diseases.[3,4] Quick detection of the COVID-19 virus (SARS-CoV-2) has become crucial for the termination of the SARS-CoV-2 infection chain. Several potential and practical detection techniques have been developed, such as reverse transcription-polymerase chain reaction (RT-PCR),[5,6] clustered regularly interspaced short palindromic repeats (CRISPR),[7] loop-mediated isothermal amplification (LAMP),[8,9] computed tomography (CT),[10] and Fourier-transform infrared spectroscopy (FTIR).[11] However, in most cases, these detection methods require a more sophisticated primer and probe design, multistep reactions, many reagents, trained technicians to run the machines, bulky instruments involving time-consuming procedures, etc.[12] The typical sensitivity of these techniques is also limited to about 81%.[13] Nevertheless, these techniques are not adequate to detect at a large scale, which is of utmost necessity to stop the spread. Therefore, developing a rapid, cheap, easy-to-use, high-accuracy, and point-of-care (POC) testing method is urgently needed. Several antigen-based test kits are being used.[14−16] Among the many antigen-based COVID-19 diagnosis methods, the field-effect transistor (FET)-based biosensors have many advantages, such as high sensitivity, ultrafast response, high selectivity, and the requirement of a small volume of analytes for the test.[17−20] FET also offers biodegradability, potential flexibility, and biocompatibility and involves low-cost fabrication.[21,22] These devices are, in most cases, fabricated on 1D or 2D structures as conducting

Received: June 19, 2022
Accepted: September 9, 2022

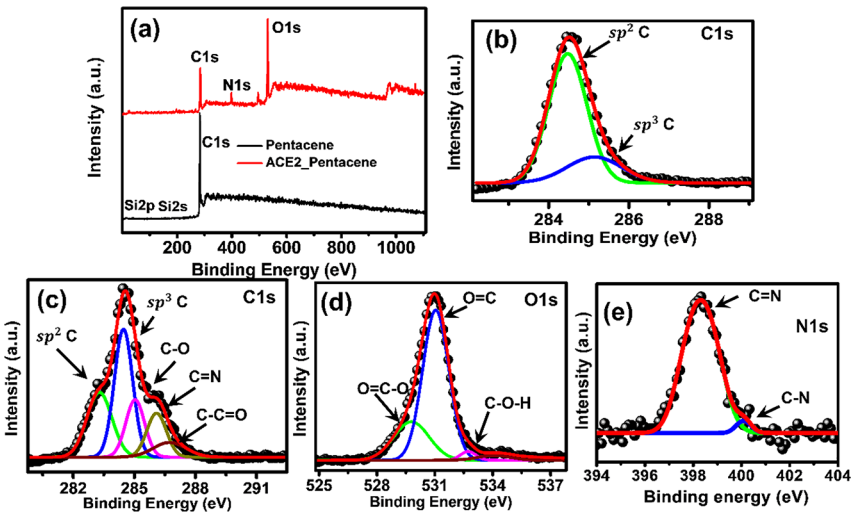

Figure 1. High-resolution XPS spectra of ACE2-coated pentacene and pentacene films on a Si substrate. (a) Wide range of the XPS spectra of pentacene and ACE2-coated pentacene films, (b) high-resolution XPS spectra of C 1s of pentacene, and (c–e) high-resolution XPS spectra of C 1s, O 1s, and N 1s of ACE2-coated pentacene films.

channels, like graphene and nanowires, which have intrinsic design complexity, leading to the impediment of scaling up for commercial uses. In addition, the functionalization by the receptor molecules of the conducting channel requires suitable chemistry to function efficiently. This work reports the integration of receptor molecules through the diffusion-induced ingress into the conducting pathway of the organic field-effect transistors (OFETs) to fabricate the SARS-CoV-2 virus directly from a saliva sample at an ultrafast rate with high selectivity.

SARS-CoV-2, a single standard RNA virus protein envelope, has a diameter of around 65–125 nm with about 30,000 nucleotides in length and four structural proteins constituting the spike surface glycoprotein (S), small envelope glycoprotein (E), matrix protein (M), and nucleocapsid protein (N).[23] The spike glycoprotein (S) cover is a transmembrane protein with a molecular weight of 150 kDa. The transmembrane spike protein (S protein) in a metastable prefusion conformation contains two functional subunits, S1 and S2. The S1 subunit binds to the host cell receptor angiotensin-converting enzyme 2 (ACE2), and the S2 subunit functions to mediate viral fusion into the host cell.[24] Transmembrane protease/serine subfamily member 2 (TMPRSS2), expressed by type II pneumocytes located on epithelial cells, cleaved the S-protein of SARS-CoV (the boundary of S1/S2 acts as a cleavage site) and promoted the virus entry. Both TMPRSS2 and ACE2 are the main determinants of SARS-CoV-2 virus entry.[25,26] The S1 subunit contains the N-terminal and receptor-binding domains (RBD) located on S1. The RBD of S1 undergoes hinge-like conformational movement in the opened or closed state, where the open status allows for receptor engagement and refolding of the S2 subunit for membrane fusion.[27] ACE2 plays an essential role in virus entry inside the cell, making the molecule a potential candidate for detecting SARS-CoV-2.[28,29] The schematic structure of ACE2-RBD is shown in Supplementary Figure S1.[30] We developed an OFET-based SARS-CoV-2 biosensor by using ACE2 as a receptor molecule. We studied the infusion of ACE2 molecules at the semiconducting/dielectric interface using diffusion through the grain boundaries of dendrite structures to let ACE2 get easy access to the conducting pathway and modulate the device current upon interactions with the spike protein of SARS-CoV-2. The diffusion of ACE2 molecules has been controlled by varying the thickness of the film. As ACE2 molecules intermingle with the pentacene molecules through grain boundaries, it naturally modifies the film's crystallographic orientation, leading to the reduction of the device current. However, we have engineered the diffusion process by controlling the thickness of the film to achieve a balance between device and sensing performances. Saliva samples collected from the patients were used for sensing the SARS-CoV-2 virus. We have observed about less than a minute of detection time with 94% sensitivity, which is the highest reported value. Saliva is a promising candidate for the diagnosis of SARS-CoV-2 virus alternative to nasopharyngeal and oropharyngeal swabs. A high viral load reduces the risk of healthcare workers getting infected during swab collection, and painless sample collection makes the saliva an attractive diagnostic tool for SARS-CoV-2. It has been experimentally studied that the viral load in saliva varies to copies per mL, and the presence of SARS-CoV-2 in saliva remains up to 24 days after COVID-19 symptoms.[31–33]

RESULTS AND DISCUSSION

ACE2 molecules are spin-coated on the pentacene film at a different rotational speed per minute (RPM) to vary the thickness of the films. X-ray photoelectron spectroscopy (XPS) measurements were carried out on these films to confirm the residual bonding and the presence of ACE2 molecules on the pentacene film. A pentacene film with a thickness of 20 nm was grown on silicon substrates for XPS measurements. Core-level binding energies of the C 1s peak were determined at 284.5 eV as the charge reference. Figure 1a shows the wide scan of the XPS spectra of pentacene and ACE2 coated on pentacene. The results demonstrated the presence of C and O in both films. However, the presence of the N peak is the signature of ACE2 molecules. Figure 1b shows the high-resolution XPS spectra of carbon of the pentacene film. The peak is deconvoluted into two compounds, one at 284.5 eV for carbon binding to (sp^2C–C) and the other at 285.2 eV attributed to sp^3C. The high-resolution core spectra of C 1s, O 1s, and N 1s on ACE2-

https://doi.org/10.1021/acssensors.2c01287
ACS Sens. XXXX, XXX, XXX–XXX

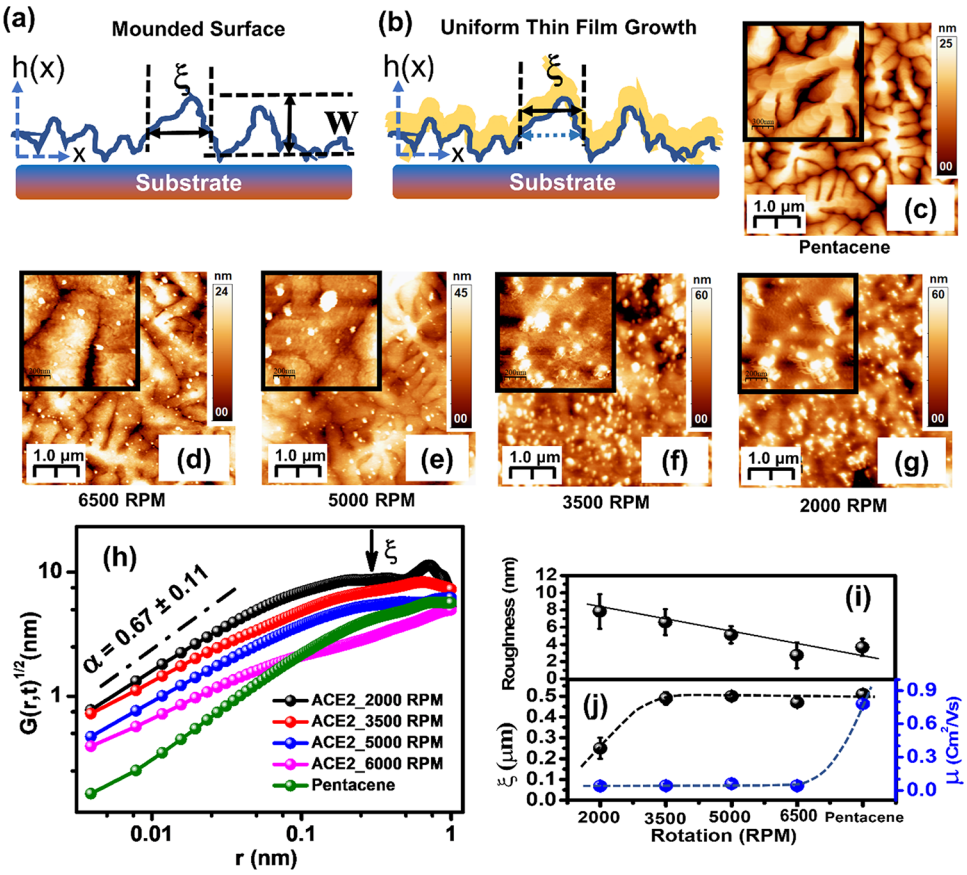

Figure 2. (a) Schematic illustration of the surface morphology of a film represented by a line profile, where W and ξ indicate the roughness and correlation length, respectively. (b) Schematic image showing the uniform growth of the second film. (c) Surface morphology of the pentacene film (5 μm × 5 μm scan area). The inset image represents the high-resolution surface morphology (1 μm × 1 μm scan area). (d–g) Surface morphologies of ACE2-coated pentacene films with different thicknesses grown at various speeds, such as 6500, 5000, 3500, and 2000 RPM. (h) Log–log plot for the height–height correlation function $G^{1/2}(r)$ vs r for the pentacene film. ACE2 films were grown on the pentacene film with different thicknesses. (i) Variation of roughness and (j) lateral correlation length (down) and mobility (blue) with the thickness of ACE2 grown on pentacene surfaces.

coated pentacene films are presented in Figure 1c–e, respectively.

The high-resolution C 1s spectra of ACE2 were fitted with five peaks as follows: (sp^2C) at 283.2 eV, carbon binding to carbon at 284.5 eV, (sp^3C) at 285.2 eV (C–O), carbon making a double bond with nitrogen (C═N) at 286.1 eV,[34] which is assigned to the amide or amine bond of ACE2, and carbon making one double bond with nitrogen and one single bond with carbon (C—C═O) at 286.7 eV,[35] which is attributed to the amide or hemiacetal of ACE2.[36] The high-resolution spectra of O 1s of ACE2 were fitted with three different peaks at 529.8, 531.05, and 532.76 eV. Two peaks at 529.8 and 532.76 eV were ascribed to mainly O═C—O and C–O–H. The O═C peak comes from the amide group of ACE2 located at 531.05 eV,[37] and a satellite peak at 534.1 eV corresponds to the water molecule H–O–H.[38] The peak at 398.1 eV represents the N 1s core level, as shown in Figure 1e, the peak is deconvoluted with two Gaussian line shapes, and the fitted peaks are located at 398.1 and 400 eV ascribed to the C═N[39] imine bond and C–N[40] amine bond, respectively. All the molecular bonds were confirmed with the chemical structure of ACE2.[41]

The uniform growth of ACE2 films can confirm better intermingling with pentacene films to achieve enhanced sensing performances on OFET-based devices. To get insight into the growth of ACE2 films, we used the statistical analysis of rough surface morphologies. Figure 2a shows a typical height fluctuation profile, $h(x)$, of mounded surfaces, with x as the lateral distance on the surfaces. The lateral correlation length (ξ) in mounded surfaces represents the average size of the mounds, as marked by an arrow in Figure 2a. W represents the interface width, indicating RMS roughness. When a film is grown on such mounded surfaces, ξ and W will vary depending on the growth modes. In the case of uniform growth, when the film closely follows the underlying surface morphology, the values of ξ remain constant, as shown in Figure 2b. A typical tapping mode AFM image of the pentacene film is shown in Figure 2c. High-resolution images in the inset reveal the formation of molecule terraces of the dendrite structures, indicating a better crystallographic molecular arrangement. The representative AFM images, with a high resolution in the inset, of ACE2 films are shown in Figure 2d–g. As we spin-coat 0.12 mg/mL ACE2 solution at different rotational speeds (2000 to 6500 RPM) on pentacene films, the molecules start filling up kinks and grain boundaries through diffusion. The AFM images clearly depict that ACE2 films follow the morphologies of underlying pentacene films at higher RPM (>5000 RPM) when the thickness of the film is less. As we reduce the RPM, the thickness of the films increases.

https://doi.org/10.1021/acssensors.2c01287
ACS Sens. XXXX, XXX, XXX–XXX

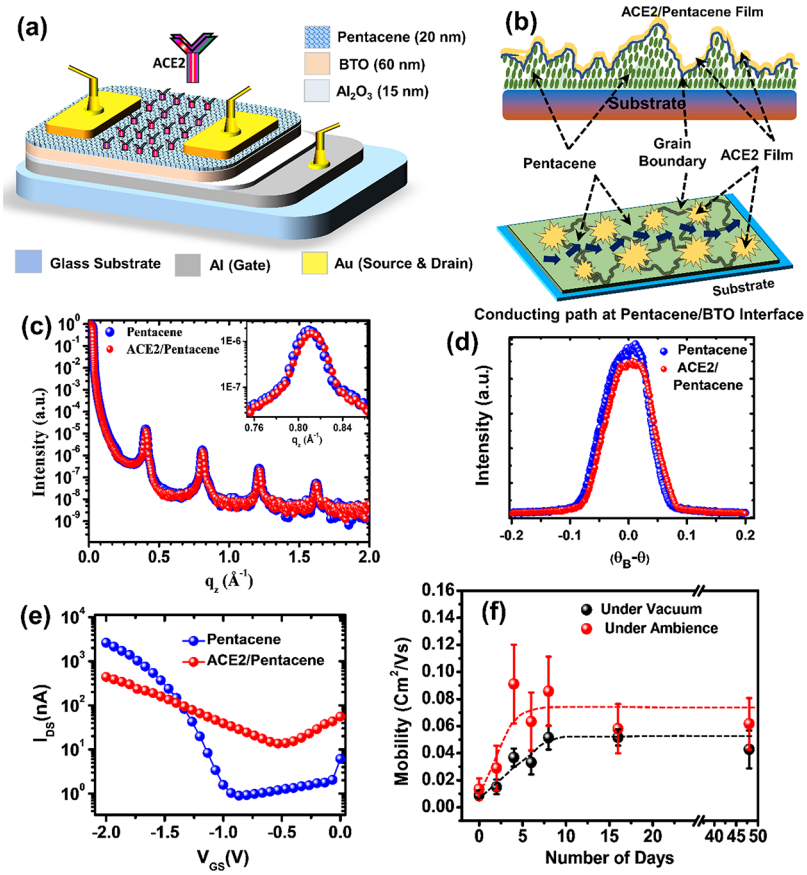

Figure 3. Device structure and performance of OFETs. (a) Schematic design of ACE2 and pentacene-based bilayer OFETs for COVID-19 sensors. (b) Cross-sectional and 2D projection of ACE2-coated pentacene on the interface showing the charge conducting pathway by arrows. The star areas indicate the direct access of ACE2 molecules at the interface. (c, d) XRR and rocking curve of pentacene and ACE2-coated pentacene films. (e) Transfer characteristic curve of pentacene and ACE2-based devices. (f) Variation of mobility with the function of time under different environmental conditions.

Therefore, the molecules start to fill up the valleys of dendrite structures and form ACE2 mounds.

Figure 2d,e represents the ACE2 film morphology for 6500 and 5000 RPM, indicating the growth of the ultrathin layer following the underlying pentacene film. The molecular steps of pentacene films are not visible except the dendrite structures, as shown in Figure 2c. To study the growth of the ACE2 films, we have calculated the height−height correlation function $G(r)$, which is defined as:[42]

$$G(r) = \langle [h(r) - h(0)]^2 \rangle \quad (1)$$

where $h(r)$ is the height of the surface at any position r for the film grown at a specific RPM. This can also be written as

$$G(r) \sim r^{2\alpha} \text{ for } r \ll \xi \sim 2W^2 \text{ for } r \gg \xi \quad (2)$$

with ξ as the lateral correlation length, W as the interface width, and α as roughness scaling exponents, whose value is $0 < \alpha < 1$ for self-affine fractal surfaces. The correlation length ξ is defined as the measurement of length beyond which the surface height is not laterally correlated. The variation of interface W and ξ with RPM is shown in Figure 2i,j, respectively. The typical calculated $G^{1/2}(r)$ values for various ACE2 film thicknesses are shown in Figure 2h. W, ξ, and α can be calculated from Figure 2h. ξ is the position of r (marked by a downward arrow in Figure 2h) at the first local minima of $G^{1/2}(r)$, and W is the value of $G^{1/2}(r)$ at the half-value of ξ, as $W = G^{1/2}(\xi/2)$. We have observed the constant value of roughness exponent α as 0.67 ± 0.11, which has been calculated from the fitting of the linear portion of the log−log plot of $G^{1/2}(r)$ vs r. Similar α values for all the film thicknesses indicate that ACE2 films follow the surface morphologies of the underlying dendritic structure of pentacene films. Such an observation is evident in the AFM images for the ultrathin film grown at 5000 and 6500 RPM. With increasing thickness of the ACE2 film grown at lower RPM, the visibility of the pentacene dendrite structure reduces (Figure 2e−g), and the roughness gradually increases from 2.7 to 8.0 nm, as represented in Figure 2i. We have fabricated OFETs using various thicknesses of ACE2-coated pentacene films. The variation of ξ with the RPM of the ACE2 films is shown in Figure 2j. There is no significant variation of correlation length up to 3500 RPM, indicating the uniform growth of ACE2 films on pentacene dendrite structures. However, films grown at 2000 RPM showed a smaller correlation length, indicating filling up of the valleys between grains. The field-effect mobilities (μ) were extracted from the transfer characteristic curves, as shown in Figure S2, of the respective OFET devices. The variation of μ with RPM is shown in Figure 2j (blue). ACE2-coated devices showed a significant reduction in carrier mobility due to changes in the crystallinity of the pentacene film upon diffusion of ACE2 molecules into the grain boundaries. Although the carrier mobility of the OFETs developed with higher ACE2 film thickness shows no significant variation in carrier mobility, as the thickness

https://doi.org/10.1021/acssensors.2c01287
ACS Sens. XXXX, XXX, XXX−XXX

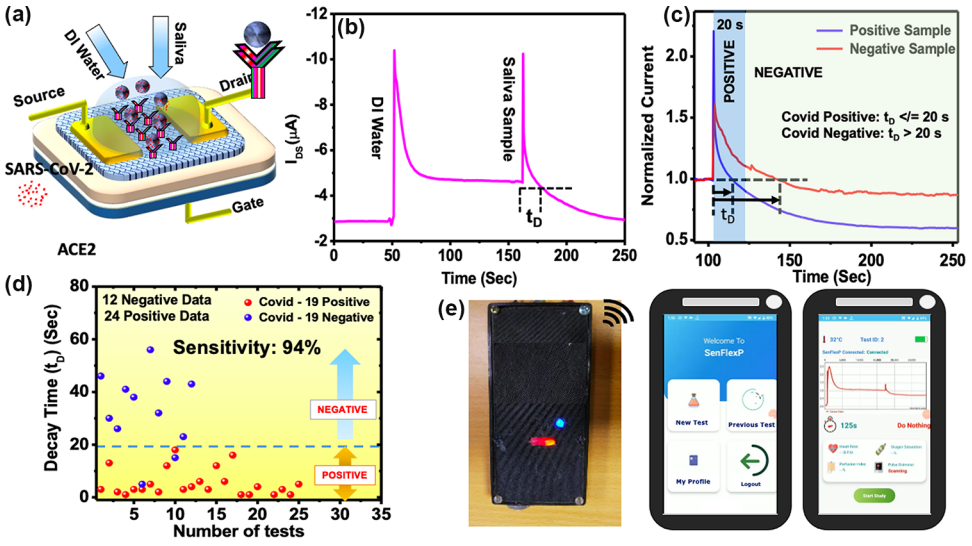

Figure 4. Detection of SARS-CoV-2 spike protein in the OFET. (a) Schematic design of the OFET indicating the steps for the detection of SARS-CoV-2. (b) Real-time variation of device current in the presence of DI water and saliva sample. (c) Variation of normalized current in the presence of COVID-positive and COVID-negative saliva samples. (d) Decay time plotted as the function of the number of tests performed. Blue and red dots represent the negative sample and positive sample, respectively. The calculated sensitivity of our device is around 94%. (e) Photograph showing the portable prototype designed for POC testing. SenFlex.P, an Android app, is developed for remotely controlling the COVID-19 test, which is connected with the prototype module via Bluetooth. The screenshot image of the SenFlex.P app during the testing is shown.

increases, the devices are supposed to offer poor sensitivity in sensing SARS-CoV-2 due to accessibility to the charge conducting path situated at the semiconductor/dielectric interface. We have selected the ACE2 film grown at 5000 RPM for final sensor fabrication because the film's thickness is low enough to increase sensitivity yet develop a better OFET device.

Figure 3a shows the schematic design of the OFET for SARS-CoV-2 detection. The device has been fabricated on a glass substrate with Al as the gate electrode. We have used a bilayer dielectric system to reduce the operating voltage as well as the leakage current. A part of the Al film has been converted into Al_2O_3 with a thickness of 15 nm using the anodization technique. A barium titanate (BTO) sol layer with a thickness of 60 nm has been spin-coated on the Al_2O_3 layer as the second dielectric layer. A 20 nm-thick thermally evaporated pentacene film spin-coated with ACE2 molecules has been used as a semiconducting channel. We used Au contacts as the source and drain grown on the pentacene film. As we coat ACE2 on the pentacene film, the molecules start diffusing into the pentacene film through the boundaries of dendrite structures, as shown in Figure 2c. Therefore, the diffused ACE2 molecules easily access the charge transfer path at the pentacene/dielectric interface. A typical cartoon representing the cross-sectional and 2D projection of ACE2-coated pentacene on the interface is shown in Figure 3b. We have achieved a uniform ultrathin ACE2 film formation at high RPM, as marked in green color, and this was confirmed from AFM analysis. The diffused ACE2 molecules through the grain boundaries are expected to modify the conducting channel, as shown in the 2D interface projection presented in Figure 3b. Blue arrows represent the conducting pathway through pentacene grains to establish the device current. A pentacene dendrite structure has two crystallographic phases (thin film and bulk) with slightly different lattice constants. To confirm if there are any crystallographic changes in the pentacene film by the diffused ACE2 molecules, we have carried out an X-ray reflectivity (XRR) measurement on these films. Figure 3c shows the typical XRR results on pentacene and ACE2-coated pentacene films. We have observed up to fourth-order Bragg's peaks, confirming an excellent vertical molecular arrangement in both the samples. The inset of Figure 3c shows the enlarged portion of second-order Bragg's peak. No significant changes in pentacene and ACE2-coated pentacene are observed. However, the rocking scan taken at the first-order Bragg's peak shows a slight shift in the peak position with a decrease in peak intensity, confirming some modification to the molecular arrangement upon diffusion of ACE2 molecules. We did not resolve Bragg's peaks for the thin-film and bulk phases on the 20 nm pentacene film. However, the minor changes reflected in the rocking scan could be due to the modification of the thin-film phase of pentacene dendrite structures. Figure 3e shows the plot of transfer curves for the OFETs developed with bare pentacene and ACE2-coated pentacene films. The threshold voltage has shifted from −1.1 to −0.6 V for the devices covered with ACE2 with a reduction in device current, and the carrier mobility decreases from 0.78 (±0.05) to 0.06 (±0.03) $cm^2/(V\ s)$ (Supplementary Figure S3). The stability of the devices is confirmed up to 50 days after fabrication. Typically, the devices kept under a vacuum desiccator showed better strength. Moreover, a significant enhancement in carrier mobility has been observed in the first 15 days, and after that, it gets saturated, as shown in Figure 3f. Such improvement in the performance of the device could be due to the rearrangement of pentacene molecules in the film.

A schematic design of the device during the sensing of SARS-CoV-2 is shown in Figure 4a. Typically, the devices are biased with $V_{DS} = -2V$ and $V_{GS} = -2V$ during sensing while continuously monitoring the I_{DS}. A drop of DI water with a volume of 1 μL is placed on the ACE2-coated pentacene channel between source and drain contacts. A typical profile of variation of I_{DS} with time is shown in Figure 4b. A small volume (1 μL) of the saliva sample is further dropped on the water droplet. The sharp increase in current when water is

https://doi.org/10.1021/acssensors.2c01287
ACS Sens. XXXX, XXX, XXX−XXX

dropped on the sensor is due to the additional proton generation from the dissociation of water molecules on the semiconducting channel's surface.[43] However, the current saturates within a few seconds. The saliva sample is dropped once the current saturates. The second peak in the device current is observed when the saliva sample is added. However, the decay of the device current significantly depends on the presence of SARS-CoV-2 in the saliva sample. We have defined a decay time (t_D) as the time when the device reaches its original current before adding the saliva sample into the water drop. The observed decay times for the sample with SARS-CoV-2 virus and without it belong to two groups. The decay time is restricted to 20 s for the samples with SARS-CoV-2 virus, which are considered COVID-positive samples. However, the decay time is always more than 20 s for the samples without any virus contents, which are regarded as COVID-negative samples. Normalized responses for COVID-positive and COVID-negative samples are shown in Figure 4c.

The S1 subunit of the spike (S) protein of SARS-CoV-2 contains a receptor-binding domain by recognizing and binding to the host receptor ACE2. In contrast, the S2 subunit mediates viral cell membrane fusion by forming a six-helical bundle via the two-heptad repeat domain. Therefore, when the S protein binds with ACE2 coated on the sensor surface, the charge accumulation at the interface is reduced. Thus, the device current decreases. The absorption of S protein is a faster process, leading to a lower decay time for positive samples. However, this decay is prolonged for the sample without SARS-CoV-2 virus for the negative samples. As shown in Figure 4c, the decay constant for a positive sample is much faster than that for the negative sample. A shorter decay time represents a higher viral load. The viral load will be zero when the decay time reaches 20 s. The decay time for 24 positive samples and 12 negative samples is shown in Figure 4d. The normalized current changes for all positive and negative samples are shown in Supplementary Figure S4. No positive samples showed false negatives, indicating higher sensor sensitivity. However, we observed two negative samples showing a positive decay time, which could be due to sample delivery or poor device functionality. We calculated about 94% sensitivity in the samples we measured. We have also compared our results with recently published research reports and devices on the COVID-19 sensors, as represented in Table S1. This confirms that our device shows an excellent sensitivity (94%) and fast response time (~20 s) compared to other COVID-19 sensors and other reported FET-based devices. We have developed a prototype module to demonstrate the functionality of the sensors for point-of-care (POC) applications. The sensor is connected to measuring electronics wirelessly connected to an Android app (SenFlex.P) through a Bluetooth connection to monitor the changes in device current during the measurement. Figure 4e shows a prototype module (SenFlex) designed to perform the sensing experiment appropriate for POC remotely. The Android app can be used for live monitoring of the sensor response and generation of the report. Using this prototype module, we have collected all the data presented in Figure 4c,d. Essential electronic elements of the prototype are shown in Supplementary Figure S5.

CONCLUSIONS

Fabrication of ultrafast SARS-CoV-2 sensors for POC application is an urgent requirement during the COVID-19 pandemic, which is yet to be ended. In this work, we have exploited the method of entering the virus into human cells through ACE2 molecules inside our mouth and the respiratory tract to fabricate highly efficient sensors with fast response. The sensors have been fabricated under the OFET platform by utilizing the grain boundaries of pentacene dendrite structures on the semiconducting channel. ACE2 molecules are used as the receptor of SARS-CoV-2 virus and have been allowed to enter through the diffusion process. The statistical analysis of the diffusion process has been studied from the variation of morphologies. We achieved less than a minute detection time in the saliva sample with about 94% sensitivity. Further, we have also demonstrated the capability of these sensors for mass testing with fewer human sources. Being sensitive to the saliva sample requires accessible sample collection and, therefore, less exposure of the healthcare staff to the virus.

EXPERIMENTAL SECTION

Materials. Angiotensin-converting enzyme 2 (ACE2) was purchased from Sigma-Aldrich and used as an active material for SARS-CoV-2 detection. ACE2 was dissolved in deionized (DI) water with a concentration of 0.12 mg/mL and stirred at room temperature in ambient conditions. Then, ACE2 solution was spin-coated on top of the pentacene film with different RPM to obtain different thickness films. The recipe for barium titanate (BTO) is described in detail in our previous paper.[22]

Fabrication of the COVID-19 Sensor. The device was fabricated on a glass substrate. First, the gate electrode Al was deposited in a thermal evaporation chamber using a shadow mask under high vacuum conditions (4×10^{-6} mbar). Then, some portion of the outer surface of the Al film was converted to Al_2O_3 using the anodization technique. Al_2O_3 was used to minimize the leakage current. The second dielectric layer, BTO, was prepared using the sol–gel method and spin-coated on Al_2O_3 at 3000 RPM for 1 min, followed by baking at 80 °C for 80 min under ambient conditions. Pentacene films (20 nm) were deposited in our custom-designed organic molecular beam deposition (OMBD) chamber at 240 °C sublimation temperature under very high vacuum conditions (2×10^{-6} mbar). Then, the ACE2 molecule was spin-coated on the pentacene film and kept in a desiccator for a few hours to evaporate the solvent. Finally, the source–drain Au electrode was deposited through a shadow mask in a thermal evaporation chamber with an active area length of 30 μm and a width of 2 mm.

Materials and Device Characterization. The crystallinity and phase confirmation of pentacene and ACE2 films were confirmed by X-ray diffraction (XRD) (Rigaku, Japan). Atomic force microscopy (AFM) (Asylum Research, Oxford Instruments) in tapping mode was used to study the surface morphology of both pentacene and ACE2 films. The chemical composition analysis of the spin-coated ACE2 film on pentacene was performed by X-ray photoelectric spectroscopy (XPS) using a PHI 5000 Versa Probe-II (ULVAC-PHI, Inc., Japan). The thicknesses of each layer of the OFET were measured using a three-dimensional optical surface profile meter (Bruker). All the electrical characterization was carried out using a Keithley 2450 SMU unit in a custom-design probe station, which works under ambient and vacuum conditions. The field-effect mobility was calculated from the saturation region of the transfer characteristic curve using eq 3.

$$I_{DS} = \frac{W}{2L} \cdot C \cdot \mu \cdot (V_{GS} - V_T)^2 \tag{3}$$

where I_{DS}, C, μ, V_{GS}, and V_T are the drain–source current, capacitance, mobility, gate-to-source voltage, and threshold voltage, respectively.

Saliva Sample Preparation. Ten milliliters of saliva was collected before or after 1 h of meal. A highly viscous saliva sample was diluted in DI water in 1:4 ratios. One microliter of the diluted saliva sample was used for testing.

https://doi.org/10.1021/acssensors.2c01287
ACS Sens. XXXX, XXX, XXX–XXX

■ ASSOCIATED CONTENT

Supporting Information

The Supporting Information is available free of charge at https://pubs.acs.org/doi/10.1021/acssensors.2c01287.

Cryo-EM structure and model of the ACE2-RBD complex, transfer characteristic curves, normalized response of all positive and negative samples, electronic circuit module, and comparison table (PDF)

■ AUTHOR INFORMATION

Corresponding Author

Dipak K. Goswami − *Organic Electronics Laboratory, Department of Physics and School of Nanoscience and Technology, Indian Institute of Technology Kharagpur, Kharagpur 721302, India;* orcid.org/0000-0002-5891-6172; Email: dipak@phy.iitkgp.ac.in

Authors

Ajoy Mandal − *Organic Electronics Laboratory, Department of Physics, Indian Institute of Technology Kharagpur, Kharagpur 721302, India*

Samik Mallik − *School of Nanoscience and Technology, Indian Institute of Technology Kharagpur, Kharagpur 721302, India*

Sovanlal Mondal − *School of Nanoscience and Technology, Indian Institute of Technology Kharagpur, Kharagpur 721302, India*

Suvani Subhadarshini − *School of Nanoscience and Technology, Indian Institute of Technology Kharagpur, Kharagpur 721302, India*

Riya Sadhukhan − *Organic Electronics Laboratory, Department of Physics, Indian Institute of Technology Kharagpur, Kharagpur 721302, India*

Tanmay Ghoshal − *Department of Electronics and Electrical Communication Engineering, Indian Institute of Technology Kharagpur, Kharagpur 721302, India*

Suman Mitra − *School of Nanoscience and Technology, Indian Institute of Technology Kharagpur, Kharagpur 721302, India*

Mousam Manna − *B C Roy Technology Hospital, Indian Institute of Technology Kharagpur, Kharagpur 721302, India*

Suman Mandal − *Organic Electronics Laboratory, Department of Physics, Indian Institute of Technology Kharagpur, Kharagpur 721302, India*

Complete contact information is available at: https://pubs.acs.org/10.1021/acssensors.2c01287

Notes

The authors declare no competing financial interest.

■ ACKNOWLEDGMENTS

This work has been partially supported by various funding agencies of the Government of India with sanction order nos. (MeitY) 5(1)/2021-NANO, (MeitY) 5(1)/2017-NANO, and (DST) DST/NM/NNetRA/2018(G)-IITKGP. We acknowledge the support provided by the XPS facility in the Department of Physics. We also want to thank Mr. Rupam Das and Mr. Ramu for their help at the time of sample collection.

■ REFERENCES

(1) Ćosić, K.; Popović, S.; Šarlija, M.; Kesedžić, I. Impact of human disasters and COVID-19 pandemic on mental health: potential of digital psychiatry. *Psychiatr. Danubina* **2020**, *32*, 25−31.

(2) El Zowalaty, M. E.; Järhult, J. D. From SARS to COVID-19: A previously unknown SARS-related coronavirus (SARS-CoV-2) of pandemic potential infecting humans−Call for a One Health approach. *One health* **2020**, *9*, No. 100124.

(3) Wong, A. W.; Fidler, L.; Marcoux, V.; Johannson, K. A.; Assayag, D.; Fisher, J. H.; Ryerson, C. J. Practical considerations for the diagnosis and treatment of fibrotic interstitial lung disease during the coronavirus disease 2019 pandemic. *Chest* **2020**, *158*, 1069−1078.

(4) Stokstad, M.; Klem, T. B.; Myrmel, M.; Oma, V. S.; Toftaker, I.; Østerås, O.; Nødtvedt, A. Using biosecurity measures to combat respiratory disease in cattle: The Norwegian control program for bovine respiratory syncytial virus and bovine coronavirus. *Front. Vet. Sci.* **2020**, *7*, 167.

(5) Corman, V. M.; Landt, O.; Kaiser, M.; Molenkamp, R.; Meijer, A.; Chu, D. K.; Bleicker, T.; Brunink, S.; Schneider, J.; Schmidt, M. L.; Mulders, D. G.; Haagmans, B. L.; van der Veer, B.; van den Brink, S.; Wijsman, L.; Goderski, G.; Romette, J. L.; Ellis, J.; Zambon, M.; Peiris, M.; Goossens, H.; Reusken, C.; Koopmans, M. P.; Drosten, C. Detection of 2019 novel coronavirus (2019-nCoV) by real-time RT-PCR. *Euro surveill.* **2020**, *25*, No. 2000045.

(6) Bwire, G. M.; Majigo, M. V.; Njiro, B. J.; Mawazo, A. Detection profile of SARS-CoV-2 using RT-PCR in different types of clinical specimens: A systematic review and meta-analysis. *J. Med. Virol.* **2021**, *93*, 719−725.

(7) Broughton, J. P.; Deng, X.; Yu, G.; Fasching, C. L.; Servellita, V.; Singh, J.; Miao, X.; Streithorst, J. A.; Granados, A.; Sotomayor-Gonzalez, A.; Zorn, K.; Gopez, A.; Hsu, E.; Gu, W.; Miller, S.; Pan, C. Y.; Guevara, H.; Wadford, D. A.; Chen, J. S.; Chiu, C. Y. CRISPR-Cas12-based detection of SARS-CoV-2. *Nat. Biotechnol.* **2020**, *38*, 870−874.

(8) Lalli, M. A.; Langmade, S. J.; Chen, X.; Fronick, C. C.; Sawyer, C. S.; Burcea, L. C.; Wilkinson, M. N.; Fulton, R. S.; Heinz, M.; Buchser, W. J.; Head, R. D.; Mitra, R. D.; Milbrandt, J. Rapid and extraction-free detection of SARS-CoV-2 from saliva by colorimetric reverse-transcription loop-mediated isothermal amplification. *Clin. Chem.* **2021**, *67*, 415−424.

(9) Zhu, X.; Wang, X.; Han, L.; Chen, T.; Wang, L.; Li, H.; Li, S.; He, L.; Fu, X.; Chen, S.; Xing, M.; Chen, H.; Wang, Y. Multiplex reverse transcription loop-mediated isothermal amplification combined with nanoparticle-based lateral flow biosensor for the diagnosis of COVID-19. *Biosens. Bioelectron.* **2020**, *166*, No. 112437.

(10) Adair, L. B., III; Ledermann, E. J. Chest CT findings of early and progressive phase COVID-19 infection from a US patient. *Radiol. Case Rep.* **2020**, *15*, 819−824.

(11) Barauna, V. G.; Singh, M. N.; Barbosa, L. L.; Marcarini, W. D.; Vassallo, P. F.; Mill, J. G.; Ribeiro-Rodrigues, R.; Campos, L. C. G.; Warnke, P. H.; Martin, F. L. Ultrarapid On-Site Detection of SARS-CoV-2 Infection Using Simple ATR-FTIR Spectroscopy and an Analysis Algorithm: High Sensitivity and Specificity. *Anal. Chem.* **2021**, *93*, 2950−2958.

(12) Gholami, M. D.; Guppy-Coles, K.; Nihal, S.; Langguth, D.; Sonar, P.; Ayoko, G. A.; Punyadeera, C.; Izake, E. L. A paper-based optical sensor for the screening of viruses through the cysteine residues of their surface proteins: A proof of concept on the detection of coronavirus infection. *Talanta* **2022**, *248*, No. 123630.

(13) He, J. L.; Luo, L.; Luo, Z. D.; Lyu, J. X.; Ng, M. Y.; Shen, X. P.; Wen, Z. Diagnostic performance between CT and initial real-time RT-PCR for clinically suspected 2019 coronavirus disease (COVID-19) patients outside Wuhan, China. *Respir. Med.* **2020**, *168*, No. 105980.

(14) Grant, B. D.; Anderson, C. E.; Williford, J. R.; Alonzo, L. F.; Glukhova, V. A.; Boyle, D. S.; Weigl, B. H.; Nichols, K. P. SARS-CoV-2 Coronavirus Nucleocapsid Antigen-Detecting Half-Strip Lateral Flow Assay Toward the Development of Point of Care Tests Using

Commercially Available Reagents. *Anal. Chem.* **2020**, *92*, 11305−11309.
(15) Gillot, C.; Douxfils, J.; Cadrobbi, J.; Laffineur, K.; Dogné, J. M.; Elsen, M.; Eucher, C.; Melchionda, S.; Modaffari, É.; Tré-Hardy, M.; Favresse, J. An Original ELISA-Based Multiplex Method for the Simultaneous Detection of 5 SARS-CoV-2 IgG Antibodies Directed against Different Antigens. *J. Clin. Med.* **2020**, *9*, 3752.
(16) Kasetsirikul, S.; Umer, M.; Soda, N.; Sreejith, K. R.; Shiddiky, M. J. A.; Nguyen, N. T. Detection of the SARS-CoV-2 humanized antibody with paper-based ELISA. *The Analyst* **2020**, *145*, 7680−7686.
(17) Li, Y.; Peng, Z.; Holl, N. J.; Hassan, M. R.; Pappas, J. M.; Wei, C.; Izadi, O. H.; Wang, Y.; Dong, X.; Wang, C.; Huang, Y.-W.; Kim, D.; Wu, C. MXene-Graphene Field-Effect Transistor Sensing of Influenza Virus and SARS-CoV-2. *ACS Omega* **2021**, *6*, 6643−6653.
(18) Seo, G.; Lee, G.; Kim, M. J.; Baek, S. H.; Choi, M.; Ku, K. B.; Lee, C. S.; Jun, S.; Park, D.; Kim, H. G.; Kim, S. J.; Lee, J. O.; Kim, B. T.; Park, E. C.; Kim, S. I. Rapid Detection of COVID-19 Causative Virus (SARS-CoV-2) in Human Nasopharyngeal Swab Specimens Using Field-Effect Transistor-Based Biosensor. *ACS Nano* **2020**, *14*, 5135−5142.
(19) Shao, W.; Shurin, M. R.; Wheeler, S. E.; He, X.; Star, A. Rapid Detection of SARS-CoV-2 Antigens Using High-Purity Semiconducting Single-Walled Carbon Nanotube-Based Field-Effect Transistors. *ACS Appl. Mater. Interfaces* **2021**, *13*, 10321−10327.
(20) Chadha, U.; Bhardwaj, P.; Agarwal, R.; Rawat, P.; Agarwal, R.; Gupta, I.; Panjwani, M.; Singh, S.; Ahuja, C.; Selvaraj, S. K.; Banavoth, M.; Sonar, P.; Badoni, B.; Chakravorty, A. Recent progress and growth in biosensors technology: A critical review. *J. Ind. Eng. Chem.* **2022**, *109*, 21−51.
(21) Mandal, S.; Roy, S.; Mandal, A.; Ghoshal, T.; Das, G.; Singh, A.; Goswami, D. K. Protein-Based Flexible Moisture-Induced Energy-Harvesting Devices As Self-Biased Electronic Sensors. *ACS Appl. Electron. Mater.* **2020**, *2*, 780−789.
(22) Mandal, S.; Banerjee, M.; Roy, S.; Mandal, A.; Ghosh, A.; Satpati, B.; Goswami, D. K. Organic Field-Effect Transistor-Based Ultrafast, Flexible, Physiological-Temperature Sensors with Hexagonal Barium Titanate Nanocrystals in Amorphous Matrix as Sensing Material. *ACS Appl. Mater. Interfaces* **2019**, *11*, 4193−4202.
(23) Florindo, H. F.; Kleiner, R.; Vaskovich-Koubi, D.; Acúrcio, R. C.; Carreira, B.; Yeini, E.; Tiram, G.; Liubomirski, Y.; Satchi-Fainaro, R. Immune-mediated approaches against COVID-19. *Nat. Nanotechnol.* **2020**, *15*, 630−645.
(24) Wang, Q.; Zhang, Y.; Wu, L.; Niu, S.; Song, C.; Zhang, Z.; Lu, G.; Qiao, C.; Hu, Y.; Yuen, K.-Y.; Wang, Q.; Zhou, H.; Yan, J.; Qi, J. Structural and Functional Basis of SARS-CoV-2 Entry by Using Human ACE2. *Cell* **2020**, *181*, 894−904.e9.
(25) Shang, J.; Wan, Y.; Luo, C.; Ye, G.; Geng, Q.; Auerbach, A.; Li, F. Cell entry mechanisms of SARS-CoV-2. *Proc. Natl. Acad. Sci.* **2020**, *117*, 11727−11734.
(26) Huang, Y.; Yang, C.; Xu, X. F.; Xu, W.; Liu, S. W. Structural and functional properties of SARS-CoV-2 spike protein: potential antivirus drug development for COVID-19. *Acta Pharmacol. Sin.* **2020**, *41*, 1141−1149.
(27) Ke, Z.; Oton, J.; Qu, K.; Cortese, M.; Zila, V.; McKeane, L.; Nakane, T.; Zivanov, J.; Neufeldt, C. J.; Cerikan, B.; Lu, J. M.; Peukes, J.; Xiong, X.; Kräusslich, H.-G.; Scheres, S. H. W.; Bartenschlager, R.; Briggs, J. A. G. Structures and distributions of SARS-CoV-2 spike proteins on intact virions. *Nature* **2020**, *588*, 498−502.
(28) Hopkins, C.; Lechien, J. R.; Saussez, S. More that ACE2? NRP1 may play a central role in the underlying pathophysiological mechanism of olfactory dysfunction in COVID-19 and its association with enhanced survival. *Med. Hypotheses* **2021**, *146*, No. 110406.
(29) Mehrabadi, M. E.; Hemmati, R.; Tashakor, A.; Homaei, A.; Yousefzadeh, M.; Hemati, K.; Hosseinkhani, S. Induced dysregulation of ACE2 by SARS-CoV-2 plays a key role in COVID-19 severity. *Biomed. Pharmacother.* **2021**, *137*, No. 111363.
(30) Bate, N.; Savva, C. G.; Moody, P. C.; Brown, E. A.; Evans, S. E.; Ball, J. K.; Schwabe, J. W. R.; Sale, J. E.; Brindle, N. P. J. In vitro evolution predicts emerging SARS-CoV-2 mutations with high affinity for ACE2 and cross-species binding. *PLoS Pathog.* **2022**, *18*, No. e1010733.
(31) Wyllie, A. L.; Fournier, J.; Casanovas-Massana, A.; Campbell, M.; Tokuyama, M.; Vijayakumar, P.; Warren, J. L.; Geng, B.; Muenker, M. C.; Moore, A. J.; et al. Saliva or Nasopharyngeal Swab Specimens for Detection of SARS-CoV-2. *N. Engl. J. Med.* **2020**, *383*, 1283−1286.
(32) Fakheran, O.; Dehghannejad, M.; Khademi, A. Saliva as a diagnostic specimen for detection of SARS-CoV-2 in suspected patients: a scoping review. *Infect. Dis. Poverty* **2020**, *9*, 100.
(33) Zhu, J.; Guo, J.; Xu, Y.; Chen, X. Viral dynamics of SARS-CoV-2 in saliva from infected patients. *J. Infect.* **2020**, *81*, E48−E50.
(34) Canevari, T. C.; Raymundo-Pereira, P. A.; Landers, R.; Benvenutti, E. V.; Machado, S. A. S. Sol−gel thin-film based mesoporous silica and carbon nanotubes for the determination of dopamine, uric acid and paracetamol in urine. *Talanta* **2013**, *116*, 726−735.
(35) Briggs, D.; Beamson, G. Primary and secondary oxygen-induced C 1s binding energy shifts in X-ray photoelectron spectroscopy of polymers. *Anal. Chem.* **1992**, *64*, 1729−1736.
(36) Rouxhet, P. G.; Misselyn-Bauduin, A. M.; Ahimou, F.; Genet, M. J.; Adriaensen, Y.; Desille, T.; Bodson, P.; Deroanne, C. XPS analysis of food products: toward chemical functions and molecular compounds. *Surf. Interface Anal.* **2008**, *40*, 718−724.
(37) Reiche, S.; Blume, R.; Zhao, X. C.; Su, D.; Kunkes, E.; Behrens, M.; Schlögl, R. Reactivity of mesoporous carbon against water − An in-situ XPS study. *Carbon* **2014**, *77*, 175−183.
(38) Chen, Y. C.; Hsu, Y. K.; Lin, Y. G.; Lin, Y. K.; Horng, Y. Y.; Chen, L. C.; Chen, K. H. Highly flexible supercapacitors with manganese oxide nanosheet/carbon cloth electrode. *Electrochim. Acta* **2011**, *56*, 7124−7130.
(39) Wang, Y.; Xie, J.; Ren, Z.; Guan, Z. H. Postsynthetically modified hydrophobic covalent organic frameworks for enhanced oil/water and CH4/C2H2 separation. *Chem. Eng. J.* **2022**, *448*, No. 137687.
(40) Andnier, A.; Chehimi, M. M.; Gallardo, I.; Pinson, J.; Vila, N. Electrochemical Oxidation of Aliphatic Amines and Their Attachment to Carbon and Metal Surfaces. *Langmuir* **2004**, *20*, 8243−8253.
(41) Clarke, N. E.; Hooper, N. M.; Turner, A. J., Chapter 100 - Angiotensin-Converting Enzyme-2. In *Handbook of Proteolytic Enzymes;* (Third Edition), Rawlings, N. D.; Salvesen, G., Eds. Academic Press: 2013; pp. 499−504.
(42) Pelliccione, M.; Lu, T.-M. *Evolution of thin film morphology: modeling and simulation*; Springer-Verlag: New York, 2008.
(43) Turetta, N.; Stoeckel, M. A.; Furlan de Oliveira, R.; Devaux, F.; Greco, A.; Cendra, C.; Gullace, S.; Gicevičius, M.; Chattopadhyay, B.; Liu, J.; Schweicher, G.; Sirringhaus, H.; Salleo, A.; Bonn, M.; Backus, E. H. G.; Geerts, Y. H.; Samorì, P. *J. Am. Chem. Soc.* **2022**, *144*, 2546.

https://doi.org/10.1021/acssensors.2c01287
ACS Sens. XXXX, XXX, XXX−XXX